



Particle-Impact Analysis of the Degree of Cluster Formation of Rutile Nanoparticles in Aqueous Solution

Kenichi Shimizu^a, Stanislav V. Sokolov^a, Neil P. Young^b, Richard G. Compton^{a*}

Received 00th January 20xx,
Accepted 00th January 20xx

DOI: 10.1039/x0xx00000x

www.rsc.org/

Cluster formation can profoundly influence the bioavailability and (bio)geochemical activity of nanoparticles in natural aquatic systems. While colloidal properties of nanoparticles are commonly investigated using light-scattering techniques, the requirement to dilute samples can affect the fundamental nature and extent of the cluster size. Hence, an alternative in-situ approach that can cover a much higher and wider concentration range of particles is desirable. In this study, particle impact chronoamperometry is employed to probe the degree of cluster formation of Alizarin Red S modified rutile nanoparticles of diameter ca. 167 nm in conditions approximating those existing in the environment. Random collisions of individual clusters of the modified rutile particles with a stationary electrode result in transient current signals during a chronoamperometric measurement, indicative of the reduction of the adsorbed Alizarin Red S dye molecules. The results from the particle-impact analysis reveal that the nanoparticles are heavily clustered with an average 91 monomeric particles per cluster. As the spherical equivalent size of the clusters (ca. 754 nm in diameter) is considerably larger than that of from nanoparticle tracking analysis (ca. 117 nm), the present work highlights the impact of the dilution on the fundamental nature of the colloidal suspension and introduces the electrochemical determination of the size distribution of inert mineral nanoparticles in highly concentrated media.

Introduction

Cluster formation via either agglomeration or aggregation is a naturally occurring process resulting from the mutual adhesion of suspended particles.^{1,2} This plays an important role in (bio)geochemical activity of mineral nanoparticles, as the increase in size affects their solubility and mobility.^{3,4} The cluster formation process also influences the cytotoxicity of nano-particulates by affecting cellular accumulation and/or penetration.^{5,6} Furthermore, for technological applications, clustering can affect efficiency of nano-catalysts by decreasing the surface-to-mass ratio, affecting the diffusion of the reactants to the surface, and/or by altering their electronic properties.^{7–10} In these respects, agglomeration, a *reversible* cluster formation that can be de-associated into monomeric particles, and aggregation, an *irreversible* cluster formation driven by strong intermolecular forces, are equally important colloidal behavior.¹¹

Among the number of analytical methods applied to detect cluster formation, dynamic light scattering and nanoparticle tracking analysis are two of the most common approaches for nanoparticle characterization owing to their simplicity of operation and the accuracy of the size determination.^{4,6,12–26}

In both techniques, a particle size distribution is derived by applying the Stokes-Einstein-Sutherland equation to the experimentally obtained diffusion coefficient.^{25,27} Dynamic light scattering technique is an ensemble technique and measures a diffusion coefficient by recording temporal fluctuations of the scattered light intensity induced by the Brownian motion of the suspended particles.²⁸ This analysis has traditionally been employed to investigate cluster formation kinetics of nanoparticles.^{22–26} However, one disadvantage is that the ability of a particle to scatter light is strongly related to its size, i.e. by the power of six of the radius.²⁹ Consequently, the resulting size distribution can be distorted by virtue of the contribution of the more intensely scattering larger particles relative to the smaller particles.^{30,31} Moreover, the size distribution can be further perturbed by severe light scattering caused by sedimentation.³² Hence, in applying dynamic light scattering, it is essential to control the concentration of particles to relatively dilute conditions (ca. 10^8 – 10^{12} particles per mL)³³ in order to reduce the probability of formation of large clusters.

Nanoparticle tracking analysis monitors the scattered light of randomly moving individual particles. The technique relies on the measurement of the root mean square of the distance which a particle diffuses in a certain time, which is related to the square root of the diffusion coefficient, and subsequently, its size in a suspension can be determined.³³ This number weighted analysis effectively prevents the size distribution from being distorted by the presence of larger and/or highly reflective particles and covers a broader size distribution range

^a Department of Chemistry, Physical and Theoretical Chemistry Laboratory, Oxford University, South Parks Road, Oxford, OX1 3QZ, UK. E-mail: Richard.Compton@chem.ox.ac.uk; Fax: +44 (0)1865 275 410; Tel: +44 (0)1865 275 957

^b Department of Materials, Oxford University, Parks Road, OX1 3PH, UK.

than dynamic light scattering.^{13,33} However, for this technique to be reliable, the particle concentration needs to be diluted to within a specified narrow range (ca. $10^7 - 10^9$ particles per mL).³³ The upper concentration threshold arises so as to avoid falsely identifying closely located single particles as a single cluster. Such a limitation poses a real disadvantage for the investigation of cluster formation behavior as the high dilution may cause an agglomerate to dissociate driven by an increase in entropy.³⁴ This, furthermore, hinders accurate understanding of the state of mineral nanoparticle clustering in, for example, natural aquatic systems where the total nanoparticle concentration can be significantly higher.³⁵ Hence, an analytical tool which can carry out the in situ monitoring of individual clusters in an aqueous suspension containing a wide range of particle concentration is desirable. Accordingly, in this paper, we investigate the use of particle-impact chronoamperometry as an alternative approach.

The principle of particle-impact chronoamperometry is based on the observation of transient current signals (spikes) as a result of the Brownian motion of a single nanoparticle colliding with a stationary microelectrode held at a sufficient overpotential to drive an electrochemical reaction on or of the colliding nanoparticle.^{36–41} If the electrochemical process is quantitative, as is often the case for the electrochemical dissolution of nanoparticles, the particle size can be derived from the integrated charge under the transient signal which is directly related to the total number of constituent redox active atoms/molecules.^{42–44} Size distributions obtained using this technique are in good agreement with conventional sizing methods as reported for example by Bartlett et al.¹⁴, Shimizu et al.⁴⁵, and Lees et al.⁴⁶ This in-situ electrochemical nanoparticle sizing method is applicable to environmental samples as demonstrated by Stuart et al.⁴³ who successfully determined the size distribution of silver nanoparticles in seawater. Furthermore, the characterizable size of as small as ca. 3 nm in radius⁴⁷, the low detectable particle concentration limit of 2.5 fM (roughly equivalent to 10^6 particles per mL)⁴⁸, and the analysis of nanoparticles in optically opaque solution⁴⁹ reported for the particle-impact technique are superior to the light scattering methods. It is therefore of high interest to examine if this electrochemical approach can be applied to systems of high particle concentration in the presence of a high degree of cluster formation.

In respect to electrically insulating and/or electrochemically inactive nanoparticles, the impact technique can be applied by functionalizing the particle surface with redox active molecules. This was previously demonstrated as a non-destructive approach to assess the particle size of silver nanoparticles⁵⁰ and the surface area of gold nanorods⁵¹ via cathodic particle-impact chronoamperometry by modifying their surfaces with 1,4-nitrothiophenol, which underwent the four-proton, four-electron reduction. This technique was also used to study the adsorption of catechol on alumina (Al_2O_3) particles.⁵² Although alumina is an electrically insulating and inert mineral, the oxidation of the adsorbed molecule can still take place upon impact owing to the diffusion of charge over the surface via electron hopping between redox centers. As a

result of charge diffusion over insulating particles complete oxidation or reduction of surface bound molecules can take place, thereby allowing quantitative sizing of the impacting particle.^{53,54} In the present paper, we use this tagging approach to study the cluster formation at high particle concentration that is outside of the range of conventional methods.

In relation to the analysis of cluster formation, proof-of-concept studies have shown that the particle-impact technique can successfully identify the presence of clustered nanoparticles as well as the dynamics of cluster formation/dissociation.^{13,14,42,55–59} In some cases^{57,58}, the presence of the clustered nanoparticles was suggested by the size distribution obtained from the impact analysis being broader than the sizes observed from the electron micrographs. Thereafter, nanoparticle tracking analysis was used to confirm the presence of such clusters. The size distribution curve from the particle-impact analysis is moreover resolved into a series of Gaussian curves from which the mean sizes is used to reveal the cluster size.^{42,57–59} The slow kinetics of cluster formation was made evident from the time-resolved anodic particle-impact analysis in the specific case of citrate-capped silver nanoparticles that showed a gradual increase in modal size by ca. 50% over a two-hour period.⁵⁸

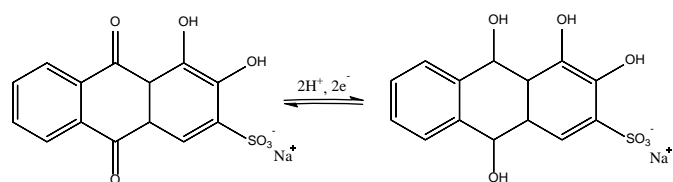
Tschulik and Compton⁵⁵ observed the formation of reversibly dissociable clusters (agglomerates) by applying a magnetic field during the cathodic particle-impact analysis of uncapped magnetite (Fe_3O_4) nanoparticles. Their work⁵⁵ showed an increase in the modal size and a broadening of the size distribution due to agglomeration that is induced by the applied magnetic field. The reversible nature of agglomeration was further shown by Sokolov et al.¹³ who demonstrated the dissociation of agglomerated citrate-capped silver particles by briefly bubbling the colloidal suspension with N_2 gas between chronoamperometric measurements. The resulting size distribution was in good agreement with that of the monomeric silver particle obtained from microscopic images, whereas that of the light scattering analysis showed a much larger modal size and broader size distribution.

The dissociation of bismuth oxide clusters was also studied using the particle-impact approach by Bartlett et al.¹⁴ In their work, uncapped bismuth oxide nanoparticles were cathodically reduced upon impact to form metallic bismuth, which was then deposited on the electrode surface. The scanning electron microscopy imaging of the electrode after the particle-impact experiment showed only the presence of monomeric bismuth particles. This suggested that only single particles reached the electrode surface even though cluster formation was evident from the nanoparticle tracking analysis. Lack of large bismuth clusters was attributed to a rapid dissociation of the faster-diffusing single particles from the slower-diffusing clusters near the electrode surface.¹⁴ Furthermore, de-agglomeration is likely promoted within the close proximity of the electrode surface as the monomeric particles are rapidly consumed by cathodic impacts.⁶⁰

The particle-impact detection of dissociated monomeric particles has also been utilized to show the effect of solution

pH on the agglomeration equilibria of hematite nanoparticles.⁵⁶ In that study, a decrease in the impact frequency and a positive shift in the mean particle size were attributed to the equilibrium shifting towards agglomeration with increasing pH, an observation consistent with the Derjaguin-Landau-Verwey-Overbeek (DLVO) theory.⁶¹ The above-mentioned reports all involved the use of the destructive Faradaic-impact approach. The novelty of the present work is the use of particle “tagging” with a redox active probe in order to explore the degree of cluster formation of a naturally occurring mineral with negligible electrical conductivity under high particle concentrations that is above the range of the conventional size-determining methods and environmentally relevant at the same time.

Rutile, which is been studied in the present work, is one of the most naturally abundant transition metal oxides and the most thermodynamically stable mineral form of titanium dioxide. It is known to exist in the form of nanoparticles, as is the case for many minerals, in the natural environment. The high surface to volume ratio of mineral nanoparticles plays a vital role in the bioavailability, mobility, retention, and reactivity of metals and organic matter in the Earth's upper crust.⁶² In addition, owing to its sustainability, chemical stability, resistance towards UV radiation, and photocatalytic property, considerable amounts of rutile are produced each year mainly as a white pigment in a range of commercial products such as paint coatings, ceramics, sunscreen, toothpaste, self-cleaning products, and food products.^{63,64} In light of newly emerging green technologies, the production of specially engineered rutile nanoparticles will very likely increase.^{65–69} Although there are no known serious adverse health effects reported for this mineral,^{70–74} studies have shown eco-toxicity including cytotoxicity and induced behavioral changes to microorganisms.^{4,5,75} Moreover it is known to photo-catalytically produce reactive oxygen species in aqueous media.^{76,77} The eventual impact of the leaching of the highly active engineered nanomaterials into the natural aquatic system on the biogeochemical cycle in the critical zone remains uncertain at present. Hence, it is of importance to investigate the intrinsic nature of rutile nanoparticles in the aquatic environment.



Scheme 1. Redox reaction of Alizarin Red S in acidic media.⁷⁸

The aim of this study is to determine the degree of cluster formation of rutile nanoparticles in aqueous solution using water soluble Alizarin Red S as a redox active tagging molecule. This compound contains a quinone group that can undergo an electrochemical reduction via a two-electron, two-proton redox reaction as displayed in Scheme 1.^{78,79} This molecule is used as the indicator to non-invasively study the nature of the

clustered nanoparticles. Experiments are conducted in 20 mM KCl supporting electrolyte solution (pH 2.0, adjusted with an equi-molar HCl solution) in order to approximate the natural ionic strength found in surface fresh water.¹⁷ The pH is maintained using hydrochloric acid to avoid the use of a buffer which could influence the colloidal behavior of rutile particles.⁸⁰ The successful application of the electrochemical particle impact technique will provide a new insight into clustering mineral nanoparticles in near natural conditions.

Experimental

Chemicals and Materials

Rutile nanoparticles were supplied by U.S. Research Nanomaterials, Inc. (99.9%, Texas, U.S.A.) and used after surface modification (see below). Potassium chloride ($\geq 99.0\%$) and Alizarin Red S (3,4-Dihydroxy-9,8-dioxo-2-athracenesulfonic acid sodium salt) were purchased from Sigma-Aldrich, Steinheim, Germany). Hydrochloric acid was purchased from Fisher ($\sim 37\%$, Loughborough, UK). The pH of 20 mM KCl solution was adjusted with small amounts of 20 mM HCl and measured with a PH 213 microprocessor pH meter (HANNA Instruments, Leighton Buzzard, UK) and a pH electrode (HI 1131, HANNA Instruments), which was calibrated daily. Nitrogen gas used to de-oxygenate the electrolytic solution was supplied by BOC Gases plc (99.998%, Guildford, UK) and was humidified by passing through traps of ultrapure water and 0.1 M NaOH. Gold macro (2.0 mm in diameter) and gold micro (11.0 μm in diameter) electrodes were supplied by Bioanalytical Systems Inc. (Stareton, UK), and a saturated calomel reference electrode (saturated KCl, SCE, 0.242 V vs. normal hydrogen electrode) was from ALS Co. Ltd. (Tokyo, Japan). Prior to the use, working electrodes were polished on aqueous slurries of 1, 0.3, and 0.05 μm alumina in the descending order of size to a mirror finish. Alumina residue was thereafter removed from the electrode surface by rinsing with excess ultrapure water and wiping with a wet tissue.

Physical characterization of rutile particles

The morphology of rutile used in this work was examined by transmission electron microscopy (TEM) using a Joel JEM-3000F field emission gun transmission electron microscope with an accelerating voltage of 300 kV. For TEM imaging, the nanoparticles pre-dispersed in ultrapure water were pipetted onto a holey carbon grid (Agar Scientific, Stansted, UK) and dried under ambient condition. Surface area and porosity of the nanoparticles were determined by measuring the N₂ adsorption/desorption isotherm using a Sorptomatic 1990 (Thermo Scientific, Waltham, USA). Prior to this analysis, granules of the rutile dry power were crushed using a mortar and pestle and then heated to 110 °C under N₂ flow for overnight to ensure the removal of the adsorbed water from the sample. Nanoparticle tracking analysis of modified and unmodified rutile nanoparticles was carried out using a NanoSight LM10 system (NanoSight, Amesbury, UK) with NTA 3.2 as an operating interface. An aqueous suspension of rutile

nanoparticles was injected into the sample chamber using a syringe and illuminated with a 638 nm laser source. Brownian motion of the light-scattering particles was recorded with a 20× magnification objective lens for 60 s with automatic exposure settings at 30 frames per second. Samples were re-dispersed using ultrasonic agitation immediately prior to this analysis. The “Methylene Blue” adsorption method^{81,82} was adapted to determine the surface area of rutile nanoparticles using Alizarin Red S, rather than Methylene Blue, as an adsorbent. The procedure involved dispersing unmodified rutile (20 mg) in 1 mL of an aqueous solution which contained 5 to 200 μM of the dye. The suspension was then vigorously mixed using a vortex mixer and was allowed to react during three intervals of 30 min ultrasonic agitation under dark conditions. Ultrasonic agitation was essential to keep the nanoparticles dispersed. Then, without any delay, the mixture was centrifuged at 14000 rpm for 10 min. The supernatant was subjected to further centrifugation for 25 min at the same speed in order to remove all the suspended rutile nanoparticles. Unreacted Alizarin Red S ($\lambda_{\text{max}} = 418 \text{ nm}$) in the supernatant was analyzed using a Shimadzu UV-spectrophotometer (UV-1800) with UV-probe 2.5 as an operating interface. Surface area was derived from the maximum adsorption concentration. The area per molecule of Alizarin Red S was calculated as $1.2 \times 10^{-14} \text{ cm}^2$ per molecule based on a molecular geometry optimization using the potential energy surface methods, which was carried out using Chem 3D (V. 15, PerkinElmer Informatics Inc.) and using the van der Waals radii⁸³ for the outermost elements.

Electrochemical analysis

All electrochemical experiments were conducted in a conventional three-electrode setup in a Faraday cage in the dark under the N_2 atmosphere. The temperature of the electrochemical cell was maintained at 25 $^\circ\text{C}$. Measurements were made with a Metrohm $\mu\text{Autolab II}$ potentiostat (Utrecht, the Netherlands) with Nova (v.1.11.2) as an operating interface. The potentiostat used in this work fully conserves the charge resulted from a particle-impact process.⁸⁴ For electrochemical analysis, rutile surface modification was carried out in a 1 mL centrifuge tube in an aqueous solution which contained about 0.1 mM Alizarin Red S per mg of the mineral. The mixture was vortex mixed and sonicated and thereafter left in the dark overnight. Unreacted dye was removed by centrifugation at 14000 rpm for 3 min after which 0.7 mL of the supernatant was replaced with ultrapure water. This cleaning process was repeated 13 times, except that the supernatant was replaced with 20 mM KCl (pH 2.0) for the last three washing cycles. By the final wash, the supernatant was clear and the modified rutile had an intense pink color.

Cyclic voltammetric analysis of dye-modified rutile was conducted by depositing a thin layer of nanoparticles on a gold macro-electrode. A small aliquot (2.0 μL) of an aqueous suspension of the dye modified nanoparticles was placed on a working electrode by drop-casting and dried under dark for at least 30 min. Once dried, the modified electrode was thoroughly rinsed with ultrapure water and placed in a

deoxygenated 20 mM KCl (pH 2.0). The potential was swept between 0.2 V and -0.5 V vs. SCE at the scan rate of 0.01 V s^{-1} . This experiment was repeated using the equal amount of unmodified rutile for comparison.

Particle-impact chronoamperometry was conducted using a well-polished gold microelectrode as the working electrode. Chronoamperograms were recorded for the duration of 50 s with a 0.5 ms measurement interval at the bias potential of between -0.5 V and 0.2 V vs. SCE. Prior to the measurement, dye modified rutile nanoparticles were dispersed in deoxygenated 20 mM KCl (pH 2.0) in an ultrasonic bath for 2 min. Subsequently, after every two measurements, the suspension was sonicated for 1 min while bubbling N_2 in order to keep particles dispersed in the suspension. At least nine chronoamperograms were collected at each potential, and over 2300 spikes were identified in total analyzed using Signal Counter software.⁸⁵

Results and discussion

In this section, the morphological characteristics of bare rutile nanoparticles used in this work are first addressed. Then, the electrochemical reduction of the adsorbed Alizarin Red S is probed using cyclic voltammetry. Subsequently, particle-impact chronoamperometry is employed to investigate the cluster formation of the dye modified rutile nanoparticles suspended in a dilute electrolyte solution. The result is compared with the size distribution obtained from the nanoparticle tracking analysis, and the effect of the particle concentration on the cluster formation is addressed.

Physical characterization of unmodified rutile nanoparticles

The morphology of unmodified rutile nanoparticles is shown in a TEM image provided in Figure 1a and appears mostly spheroidal and non-porous. The clustering of the nanoparticles observable in the micrograph was likely a result of the drying process and does not in itself necessarily suggest particle agglomeration/aggregation in aqueous suspension. An average diameter was estimated to be 167 (± 79) nm based on 72 rutile particles that were identified from the electron micrographs (Figure 1a). The result of the N_2 adsorption isotherm suggested a BJH (Barrett-Joyner-Halenda) pore volume of $0.022 \pm 0.002 \text{ cm}^3 \text{ g}^{-1}$ and a porosity (i.e. the ratio of the pore volume over the total volume⁸⁶) of about 9% for this metal oxide nanoparticle. A BET (Brunauer-Emmett-Teller) surface area of the nanoparticles was found to be $6.5 \pm 0.03 \text{ m}^2 \text{ g}^{-1}$. A similar value was observed from the surface area estimated using the dye adsorption method ($2.7 \text{ m}^2 \text{ g}^{-1}$). The nanoparticle tracking analysis of 5 mg L^{-1} unmodified rutile dispersed in ultrapure water revealed a log-normal distribution of the particle size with a mean diameter of 74 ($\times/2.5$) nm (Figure 1b). For a log-normal distribution, the confidence interval is reported with a sign “ $\times/$ ” to indicate that it is obtained by multiplying or dividing the log-normal mean by the standard deviation, as compared to “ \pm ” of a normal distribution.⁸⁷ The difference in the mean particle size observed in the TEM and nanoparticle tracking analyses is

likely partly due to the non-spherical particle shape, as depicted in the TEM image. This is also pointed out by the difference in the surface area estimated from the size obtained from nanoparticle tracking analysis using a hard-sphere model ($19 \text{ m}^2 \text{ g}^{-1}$) and the BET result. The results of the NTA analysis for the dilute unfunctionalised and Alizarin Red S capped particles were virtually identical (See supplementary material Figure S1). As a result we believe that coverage used in the present work does not have a significant impact on the agglomeration or aggregation state of the particles and allows us to use the functionalization method in further experiments.

Attempts were made to characterize the cluster size of dye-modified rutile nanoparticles at high concentrations using dynamic light scattering or nanoparticle tracking analysis. It was found that at a concentration of 0.1 g L^{-1} (roughly equivalent to 10^{10} particles), sedimentation, as well as adhesion of the dye modified rutile particles to the cell walls, made it impossible to carry out the size determination using light scattering methods. Analysis of cluster formation under an optical microscope (both light and dark field approaches) was also not successful because of particle sedimentation and induced cluster formation as the solvent evaporated. These attempts highlight that conventional analytical methods lack the ability to determine cluster sizes in the high particle concentration condition, which can be found commonly in natural aquatic systems.

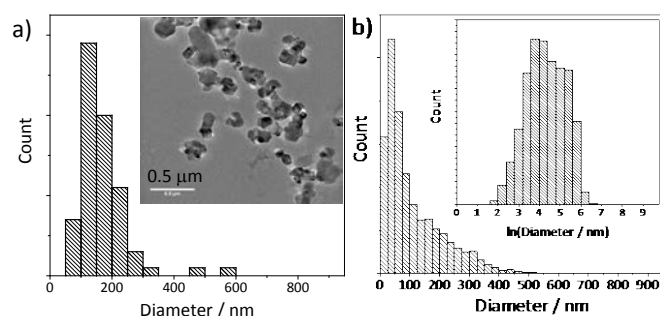


Figure 1. (a) TEM image of unmodified rutile particles (the scale bar indicates $0.5 \mu\text{m}$) along with a histogram that depicts the size distribution of 72 individual rutile nanoparticles identified in TEM images. The mean particle size is found to be $167 \pm 79 \text{ nm}$ in diameter. (b) Nanoparticle tracking analysis derived size distribution of unmodified rutile nanoparticles that were dispersed in ultrapure water (5 mg L^{-1} , which is equivalent to ca. $4.8 \times 10^8 \text{ particles mL}^{-1}$). The inset shows the distribution of the natural log of particle size. The log-mean diameter is $74 (\times/2.5) \text{ nm}$.

Cyclic voltammetric characterization of dye-modified rutile

The electrochemical activity of unbound, free Alizarin Red S is first studied under the same experimental conditions as the particle-impacts are conducted in order to properly assess the redox behavior of the molecule adsorbed on the rutile surface. Cyclic voltammograms recorded at the bare gold macro electrode in 20 mM KCl/HCl solution at pH 2.0 containing $71.2 \mu\text{M}$ Alizarin Red S show a single cathodic peak at ca. -0.30 V vs. SCE and an anodic peak at ca. -0.27 V vs. SCE (Figure 2). The peak current ratio is roughly unity, and the peak-to-peak separation of ca. 30 mV is in close agreement with $57/n \text{ mV}$ (which n is the number of electrons) for a two-electron

reversible redox reaction.⁸⁸ The peak current is also found to increase with the square root of scan rate (Figure 2 inset) indicating that the electrochemical process is diffusion controlled. Based on the linear function, the number of electrons transferred is further confirmed using the Randles-Ševčík equation:^{88,89}

$$i_p = 0.4463nFAC^b \sqrt{\frac{nFDv}{RT}} \quad (1)$$

where i_p is the peak current, n is the number of electrons involved in the redox reaction, F is Faraday constant ($= 96485 \text{ C}$), A is the electrode surface area ($= 0.031 \text{ cm}^2$), C^b is the bulk concentration of Alizarin Red S ($= 71.2 \mu\text{M}$), D is the diffusion coefficient of the dye ($= 4.3 \times 10^{-6} \text{ cm}^2 \text{ s}^{-1}$)⁹⁰, v is the scan rate, R is the gas constant ($= 8.314 \text{ J mol}^{-1} \text{ K}^{-1}$), and T is temperature ($= 298 \text{ K}$). Solving the above equation provides the n value of $2.3 (\pm 0.2)$ electrons.

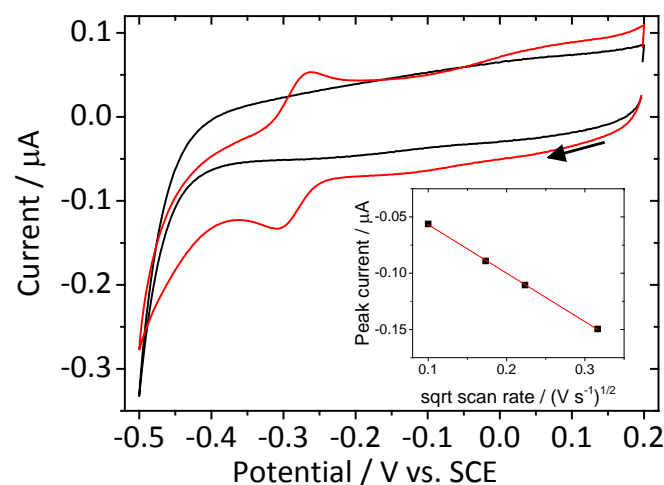


Figure 2. Cyclic voltammograms of bare Au macro electrode in 20 mM KCl at pH 2.0 with $71.2 \mu\text{M}$ Alizarin Red S (red line) and without the redox active molecule (black line) recorded at a scan rate of 0.01 V s^{-1} . An arrow indicates the direction of scan. Inset: Cathodic peak current as a function of the square root of scan rate. A red line indicates the best-fit line.

The electrochemical activity of the dye adsorbed on the TiO_2 nanoparticles was examined using cyclic voltammetry by drop-casting the dye-modified rutile nanoparticles onto a gold macro electrode and dried for at least 30 min in the dark condition. Cyclic voltammograms were recorded on the nanoparticles/gold electrode system in degassed 20 mM KCl solution at pH 2.0 at a scan rate of 0.01 V s^{-1} . The results were then compared with the cyclic voltammograms of the unmodified rutile nanoparticles/gold electrode system. The characteristic cyclic voltammograms shown in Figure 3 were generated with a nanoparticle coverage of 0.29 mg cm^{-2} on the working electrode (roughly an average of six monolayers of the nanoparticles on the electrode surface). The cyclic voltammetric response of the unmodified rutile/gold system (Figure 3, blue line) is very similar to that of the bare gold electrode system (Figure 3, black line) suggesting that rutile is not electrochemically active in the applied potential region.

For the dye modified rutile nanoparticle/glassy carbon system, cyclic voltammogram shows a cathodic peak at -0.4 V vs. SCE attributable to the reduction of the adsorbed Alizarin Red S. The anodic reverse reaction is significantly slower than the forward cathodic reaction as evidenced by the much broader oxidation peak in Figure 3. This is possibly because the electrochemical process is retarded by the loss of electrical contact between the particle and the electrode. Nevertheless, it is oxidized back to the original state by the end of a scan, as the successive scans produced the same voltammogram as shown in the figure.

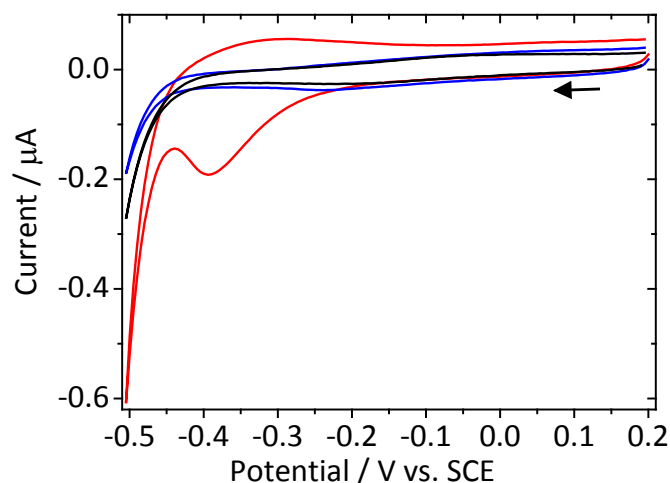


Figure 3. Cyclic voltammetric responses of the Alizarin Red S modified rutile (red), unmodified rutile (blue), and bare gold electrode (black) in 20 mM KCl (pH 2.0). The amount of both dye-modified and unmodified rutile nanoparticles used to obtain the cyclic voltammograms were 0.29 mg cm^{-2} (roughly equivalent to six monolayers of nanoparticles on the electrode surface). The measurement was made at a scan rate of 0.01 V s^{-1} . An arrow indicates the direction of the scan.

The scan rate dependent voltammetric response of the adsorbed dye molecule is further examined by varying the scan rate from 0.001 V s^{-1} to 0.1 V s^{-1} , and the resulting cyclic voltammograms collected with 0.29 mg cm^{-2} dye modified rutile are shown in Figure 4a. An arrow in the figure indicates that the scan rate was lowered in the order of 0.1 V s^{-1} , 0.07 V s^{-1} , 0.05 V s^{-1} , and 0.01 V s^{-1} . Moreover, the cyclic voltammograms recorded at 0.005 V s^{-1} and 0.001 V s^{-1} are shown in the inset of the figure. A cathodic peak is identifiable for scan rates below 0.07 V s^{-1} , and the peak current and potentials are plotted against the scan rate in Figure 4b. It is found that the peak current varies in direct proportion to the scan rate, and the peak potential shows a direct correlation with the log of scan rate (Figure 4b). These results are characteristic to the cyclic voltammetric responses of the surface bound process,⁸⁹ which is expected from a drop-cast experiment during which the electroactive elements are fixed in the confined space near the electrode surface, and the electron transfer to the adsorbed dye is electrochemically irreversible.

Considering that the electrochemical process under investigation is irreversible, the linear function between the

cathodic peak current and the scan rate can be expressed as^{88,89,91}

$$i_p = \frac{(n' + \beta)nF^2\Gamma^*Av}{2.718RT} \quad (2)$$

where n' indicates the number of electrons transferred prior to the rate-determining step, β is the transfer coefficient of the rate-determining step, Γ^* is the surface coverage in moles of the dye molecule per geometrical surface area of the working electrode, and i_p , n , F , A , v , R , and T are as defined before.

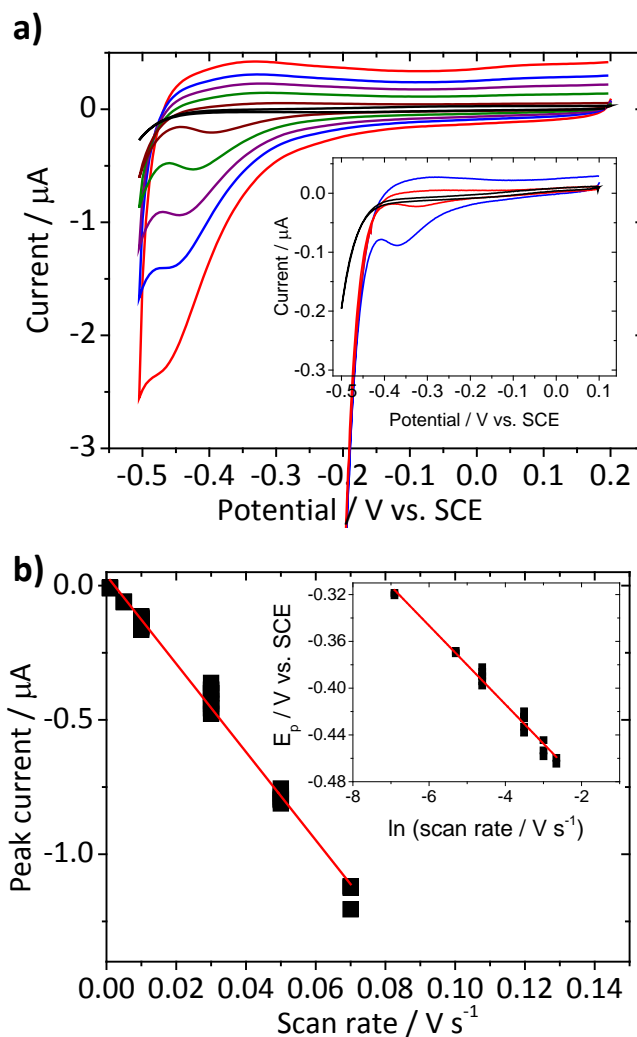


Figure 4. (a) Cyclic voltammetric responses of the dye modified rutile on a gold macro-electrode in 20 mM KCl at pH 2.0 at scan rates of 0.1 V s^{-1} , 0.07 V s^{-1} , 0.05 V s^{-1} , and 0.01 V s^{-1} . An arrow indicates the descending order of the scan rates. The voltammetric response of bare working electrode recorded at 0.01 V s^{-1} is shown with black. The inset shows the cyclic voltammogram recorded at 0.005 V s^{-1} (blue) and 0.001 V s^{-1} (red) as well as that of bare working electrode recorded at 0.001 V s^{-1} (black). The amount of the dye modified rutile nanoparticles used to obtain the cyclic voltammograms was 0.29 mg cm^{-2} . (b) Peak current as a function of scan rate. Inset: peak potential, E_p , as a function of the natural log of scan rate. Red lines indicate the best linear fits.

From the above equation, once $(n' + \beta)$ is determined, the surface coverage of the dye molecule can be calculated. This was realized by the Tafel analysis of a section of a cyclic voltammogram of the dye modified rutile/gold system which the voltammetric response is kinetically limited (Figure 5).

Upon re-plotting the highlighted section of Figure 5 in accordance to the below equation⁸⁸ a linear function is obtained (Figure 5 inset).

$$\ln|i| = \text{constant} - \frac{(n' + \beta)FE}{RT} \quad (3)$$

In the above equation, E is the applied potential and the other symbols are as defined earlier. From the slope, a $(n' + \beta)$ value of $0.47 (\pm 0.03)$ is obtained. As n' must be an integer greater than zero while β is between zero and unity, the result points to $n' = 0$ showing that the first electron transfer is the rate determining step.

By applying the $(n' + \beta)$ value of 0.47 to Eqn. 2, the surface coverage of $4.0 \times 10^{-10} \text{ mol cm}^{-2}$ is obtained. As the surface coverage given by Eqn. 2 indicates the moles of Alizarin Red S over the geometrical surface area of the gold electrode, it is converted to the dye coverage on a single rutile particle by employing the below equation:

$$\Gamma = \frac{\Gamma^* N_A}{w_t m} \quad (4)$$

where Γ is the molecular coverage of a rutile nanoparticle by Alizarin Red S, Γ^* is as defined earlier, w_t is the loading of dye-modified rutile drop-casted onto a gold electrode ($= 0.29 \text{ mg cm}^{-2}$), N_A is Avogadro's number ($= 6.022 \times 10^{23} \text{ mol}^{-1}$), and m' is a monolayer capacity⁹² which is the ratio of the BET surface area ($= 6.5 \text{ m}^2 \text{ g}^{-1}$) over the molecular cross sectional area of Alizarin Red S ($= 1.2 \times 10^{-18} \text{ m}^2$ per molecule, estimated using Chem 3D software). By solving the above equation, the molecular coverage of $0.15 (\pm 0.02)$ monolayers of the dye is found to be present at the rutile surface.

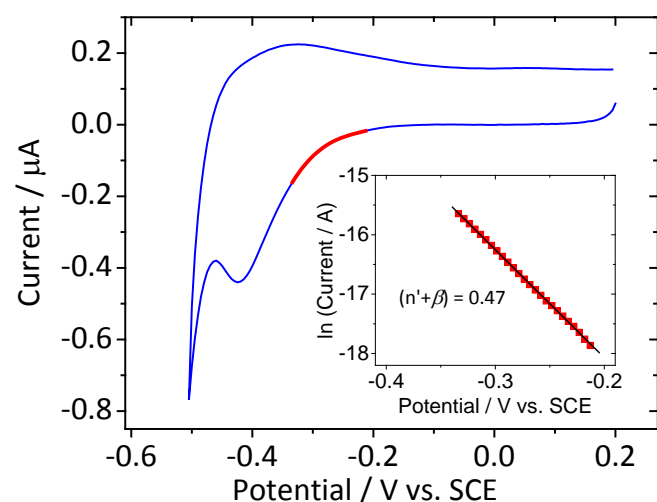


Figure 5. Baseline corrected cyclic voltammetric response of Alizarin Red S modified rutile nanoparticle deposited on a gold electrode (0.29 mg cm^{-2}) in 20 mM KCl at pH 2.0 at a scan rate of 0.03 V s^{-1} . The section of the figure which is highlighted with red is used for Tafel analysis shown in the inset. The black line in the inset is the best fit line from which the $(n' + \beta)$ value of 0.47 was calculated.

The surface coverage of Alizarin Red S on rutile nanoparticles is also derived by fitting a voltammetric response of the dye reduction with the Laviron's equation:⁹¹

$$i = \frac{(n' + \beta)nF^2}{RT} v A \Gamma^* \exp(\exp(-aE_i + g)) \exp(-aE + g) \exp(-\exp(-aE + g)) \quad (5)$$

where E_i indicates the initial applied potential, a and g are defined as

$$a = \frac{(n' + \beta)F}{RT}, \quad g = \ln \frac{k_f^0}{av} \quad (6)$$

where k_f^0 is the cathodic heterogeneous rate constant which has a unit of s^{-1} for the surface bound species.⁸⁹ The other symbols are as defined earlier. The curve fitting of the cathodic voltammetric wave using Eqn. 5 was carried out between -0.1 V and -0.46 V vs. SCE, and the parameters, $(n' + \beta)$, Γ^* , and k_f^0 are extracted. Origin Lab Pro® software (OriginLab Co., Northampton, USA) was employed to perform nonlinear least squares regression using the Levenberg-Marquardt algorithm. The resulting curve overlaying the original voltammogram is presented in Figure 6. Calculated voltammetric response is in excellent agreement with the experimental result with the correlation coefficient (R^2) of 0.9998. The cathodic rate constant, k_f^0 , was found to be $2.3 (\pm 0.4) \times 10^{-4} \text{ s}^{-1}$. The $(n' + \beta)$ value of $0.48 (\pm 0.01)$ is in good agreement with the earlier analysis of 0.47. The surface coverage was found to be $4.0 (\pm 0.1) \times 10^{-10} \text{ mol cm}^{-2}$; this value is converted using Eqn. 4 to give the molecular coverage of $0.15 (\pm 0.004)$, which is identical to the previous analysis. The results above show that the dye molecules adsorbed on the rutile particle can undergo a two-electron reduction, which is important for cluster size determination via particle impact chronoamperometry.

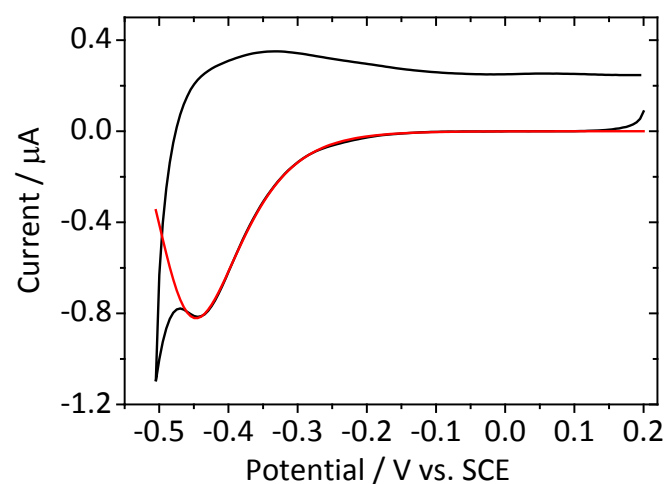


Figure 6. The calculated cyclic voltammetric response based on Eqn. 5 (red) overlaying the experimentally obtained and baseline corrected cyclic voltammogram of the dye modified rutile drop-casted on a gold electrode recorded in 20 mM KCl at pH 2.0 at a scan rate of 0.05 V s^{-1} (black).

Agglomeration behavior of dye-modified rutile nanoparticles

Cathodic particle impact chronoamperometry was conducted in a deaerated aqueous 20 mM KCl solution at pH 2.0 (adjusted to by equimolar hydrochloric acid) with the particle

concentration of between 3.2 g L^{-1} and 2.8 g L^{-1} . Chronoamperograms that were recorded in the presence and absence of the Alizarin Red S modified rutile nanoparticles are shown in Figure 7. Spikes such as the one shown in the inset of the figure only appear when the nanoparticles are present in the solution, indicating the reduction of the adsorbed dye modified at a stationary gold microelectrode. The difference in base currents between the two conditions in Figure 7 is attributable to the background reduction reaction which was taking place concurrently with the particle-impact at the gold microelectrode as a result of the presence of trace oxygen despite rigorous outgassing.

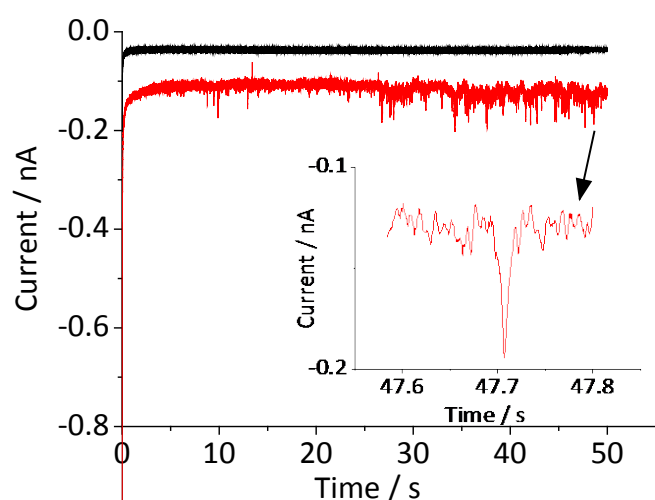


Figure 7. Characteristic chronoamperogram recorded in deoxygenated aqueous suspension of the Alizarin Red S modified rutile nanoparticles in 20 mM KCl at pH 2.1 using a gold microelectrode and at an applied potential of -0.4 V vs. SCE. The inset provides an enlarged view of a transient current-time signal resulted from the reduction of the adsorbed dye which takes place upon particle-electrode collision.

The charge passed during the impact is obtained by integrating the area under the transient signal. The histogram of the integrated charges under transient signals collected at -0.4 V vs. SCE shows the log-normal distribution (Figure 8a). Such distribution manner was found from all the potentials tested in this study, and the log-normal average charges are summarized in Figure 8b. The figure shows the maximum charge is found at bias potential between -0.5 V and -0.3 V vs. SCE. This is followed by a gradual decrease due to insufficient driving force for the electrochemical process.^{44,45,93} Impacts observed at -0.1 V vs. SCE or more positive are attributable to the capacitance of clustered nanoparticles, as the potential is not sufficient enough to drive the cathodic reduction of Alizarin Red S as well as the transient signal of similar intensity was observed from the unmodified rutile particles (Figure 8b, red markers). Hence the capacitive charge is subtracted to ensure only the charge associated with the reduction of the dye molecule is considered (Figure 8b inset).

The equation below is used to determine the degree of cluster formation, D_c :

$$D_c = \frac{q}{Q_{mono}} \quad (7)$$

where Q is the faradaic charge obtained from the particle impact experiment. Q_{mono} is expected faradaic charge from a single dye modified rutile particle (referred herein as monomer), which is derived from the following equation:

$$Q_{mono} = \Gamma \frac{4\pi ne}{S_{ARS}} r^2 \quad (8)$$

where Γ and n are as defined earlier, r is the radius of unmodified rutile nanoparticles, S_{ARS} is the molecular cross sectional area of Alizarin Red S ($= 1.2 \times 10^{-18} \text{ m}^2$), and e is the

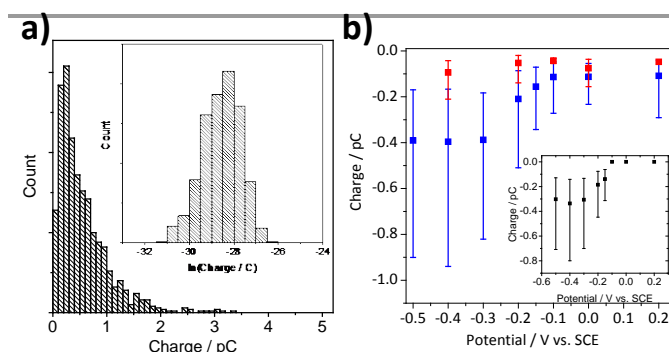


Figure 8. (a) Histogram of the charge extracted from spikes resulted from chronoamperometric measurements in deoxygenated 20 mM KCl (pH 2.0) at -0.4 V vs. SCE. (b) The log-normal average of reductive charges from dye modified rutile nanoparticles as a function of the applied potential (blue). Results from the capacitive impact of unmodified rutile are shown with red. Inset: reductive charges after subtracting capacitive charge. Error bars indicate the standard deviation.

elemental charge ($= 1.602 \times 10^{-19} \text{ C}$). Based on the mean particle size found from the electron micrograph (i.e., $2r = 167 \text{ nm}$), the expected charge of a monomer is $3.6 \times 10^{-15} \text{ C}$ (a hard-sphere model was adopted for simplicity). From the mean charge observed from the particle-impact experiment, the degree of cluster formation is calculated to be $91 (\times/2.6)$ monomers. A histogram of the degree of cluster formation is presented in Figure 9. Since the colloidal suspension was sonicated every two chronoamperometric measurements, agglomerates are generally expected to be dissociated during the electrochemical analysis.¹³ The clusters found in the present system may, therefore, be considered as an indication of aggregation although, because of the high particle concentration, it is possible that particles are rapidly agglomerating.

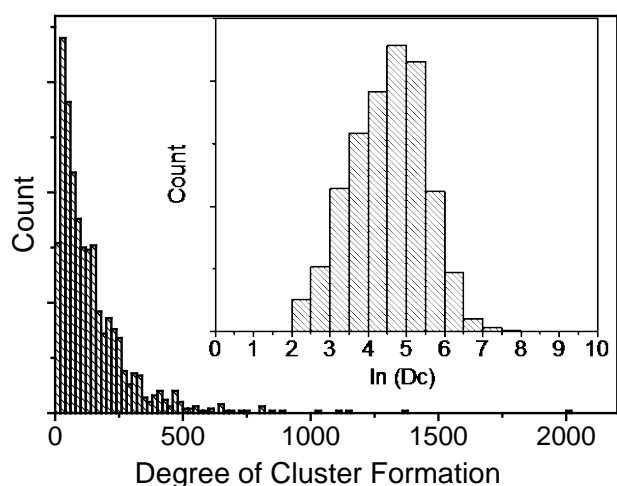


Figure 9. Histogram of the degree of cluster formation derived from the Faradic charges using Eqn. 7. The inset shows the distribution of natural log of the degree of cluster formation. The log-mean average is found to be 91 ($\times/2.6$) monomers.

To compare the results obtained from the particle-impact with that from nanoparticle tracking analysis, cluster size is estimated assuming that the volume of a cluster is proportional to that of the monomer by the degree of particle cluster formation (Eqn. 9).

$$V_{\text{cluster}} = D_c V_{\text{monomer}} \quad (9)$$

where V denotes the volume and D_c is the degree of cluster formation as defined in Eqn 7. This can be simplified to

$$r_{\text{cluster}} = D_c^{1/3} r_{\text{monomer}} \quad (10)$$

where r is the radius. By using the mean particle size from the TEM image as r_{monomer} , cluster size is found to be roughly equivalent to a spherical particle of 754 ($\times/1.4$) nm in diameter (Figure 10). In comparison, the nanoparticle tracking analysis showed a much lower degree of cluster formation, i.e. 117 ($\times/2.0$) nm in diameter, which is comparable to the size of monomeric particles found in the TEM images. The discrepancy in the two analyses is great (Figure 10) even considering the probable error due to the oversimplification of the shape of clusters when calculating the mean size from the degree of cluster formation. This is, therefore, attributable to the reversible nature of cluster formation regarded as agglomeration that affected the cluster size by shifting the equilibria towards de-agglomeration as the particle concentration is lowered for the nanoparticle tracking analysis (ca. 25 mg L⁻¹ or ca. 2.4×10^9 monomeric particles mL⁻¹ in comparison to ca. 3 g L⁻¹ or ca. 2.9×10^{11} monomeric particles mL⁻¹ for the electrochemical analysis).⁶⁰ The difference in the two analyses highlights the potential impact of sample preparation on colloidal nanoparticles in natural samples and the ability of the particle-impact chronoamperometry to obtain the size distribution from a suspension of high particle concentration.

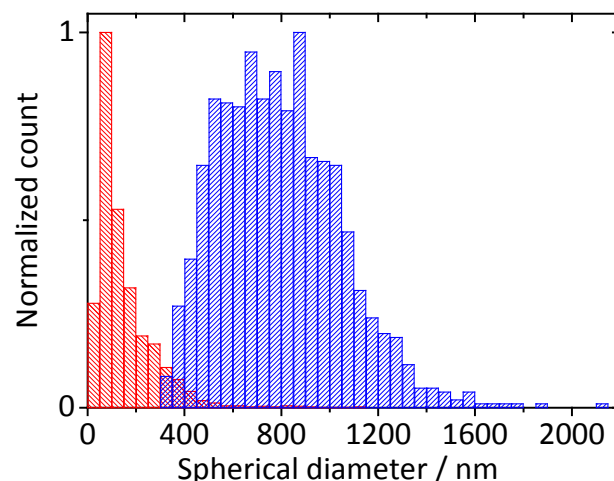


Figure 10. Histogram comparing the size distribution of the dye modified rutile nanoparticles obtained via the nanoparticle tracking analysis (red) and from the particle-impact chronoamperometry using a hard-sphere model (blue). The light scattering analysis was carried out with the concentration of ca. 25 mg L⁻¹, which is roughly equivalent to ca. 2.4×10^9 monomeric particles mL⁻¹, as compared to the particle concentration of ca. 3 g L⁻¹ (ca. 2.9×10^{11} monomeric particles mL⁻¹) for the electrochemical analysis. The histogram is normalized to have the maximum count of unity. Size distribution based on the nanoparticle tracking analysis (red) exhibits the mean value of 117 ($\times/2.0$) nm, whereas that from the particle-impact (blue) has the mean value of 754 ($\times/1.4$) nm.

Conclusions

In this study, the particle-impact chronoamperometry is employed to examine the degree of cluster formation of rutile nanoparticles in a colloidal suspension with a high particle concentration using a particle surface tagging molecule as a redox indicator. Transient signals are observed during the electrochemical analysis as the adsorbed dye molecule undergoes Faradaic reduction upon a random collision between a clustered nanoparticle and a gold microelectrode. The mean cluster size of the dye modified rutile nanoparticle obtained from the particle-impact experiment is found to be 91 ($\times/2.6$) monomers. Furthermore, the approximate spherical size of clusters is 754 ($\times/1.4$) nm in diameter, which is considerably larger than the nanoparticle tracking analysis suggested. This discrepancy is attributed to the reversible nature of cluster formation which shifted the equilibria away from agglomeration when the colloidal suspension is diluted for the light scattering analysis. The successful application of the particle-impact approach demonstrated herein offers an alternative approach for the more accurate analysis of nanoparticle clustering behavior in the natural aquatic environment. In addition, the present work highlights the complexity of the clustering process and the necessity of application of multiple characterization techniques in order to accurately characterize the system.

Acknowledgements

This work was supported by a Marie Skłodowska-Curie Intra-European Fellowships (# 626320) (KS) and the European Research Council (FP/2007-2013/ERC Grant Agreement no. [320403]) (SVS) within the 7th European Community Framework Programme. Authors thank Dr. A. Shepherd of the Surface Analysis Facility at Oxford University for the N₂ adsorption isotherm analysis.

Notes and references

- 1 J. Lyklema, H. P. van Leeuwen and M. Minor, *Adv. Colloid Interface Sci.*, 1999, **83**, 33–69.
- 2 M. Boström, V. Deniz, G. V. Franks and B. W. Ninham, *Adv. Colloid Interface Sci.*, 2006, **123–126**, 5–15.
- 3 A. L. Dale, E. A. Casman, G. V. Lowry, J. R. Lead, E. Viparelli and M. Baalousha, *Environ. Sci. Technol.*, 2015, **49**, 2587–2593.
- 4 D. Zhou, Z. Ji, X. Jiang, D. R. Dunphy, J. Brinker and A. A. Keller, *PLoS One*, 2013, **8**, e81239.
- 5 A. Simon-Deckers, S. Loo, M. Mayne-L'hermite, N. Herlin-Boime, N. Menguy, C. Reynaud, B. Gouget and M. Carrière, *Environ. Sci. Technol.*, 2009, **43**, 8423–8429.
- 6 A. Lankoff, W. J. Sandberg, A. Wegierek-Ciuk, H. Lisowska, M. Refsnes, B. Sartowska, P. E. Schwarze, S. Meczynska-Wielgosz, M. Wojewodzka and M. Kruszewski, *Toxicol. Lett.*, 2012, **208**, 197–213.
- 7 L. N. Lewis, *J. Am. Chem. Soc.*, 1990, **112**, 5998–6004.
- 8 M. Inaba, H. Yamada, J. Tokunaga and A. Tasaka, *Electrochem. Solid State Lett.*, 2004, **7**, A474–A476.
- 9 O. M. Wilson, M. R. Knecht, J. C. Garcia-Martinez and R. M. Crooks, *J. Am. Chem. Soc.*, 2006, **128**, 4510–4511.
- 10 M. Ma, Y. Zhang and N. Gu, *Colloids Surf. A*, 2011, **373**, 6–10.
- 11 A. D. McNaught, A. Wilkinson, M. Nic, J. Jirat, B. Kosat and A. Jenkins, Eds., *IUPAC. Compendium of Chemical Terminology, 'IUPAC Gold Book'*, Blackwell Scientific Publications, Oxford, 2nd edn., 2007, vol. 79.
- 12 A. B. Krueger, P. Carnell and J. F. Carpenter, *J. Pharm. Sci.*, 2016, **105**, 1434–1443.
- 13 S. V. Sokolov, K. Tschulik, C. Batchelor-McAuley, K. Jurkschat and R. G. Compton, *Anal. Chem.*, 2015, **87**, 10033–10039.
- 14 T. R. Bartlett, S. V. Sokolov, J. Holter, N. Young and R. G. Compton, *Chem. Eur. J.*, 2016, **22**, 7408–7414.
- 15 R. D. Boyd, S. K. Pichaimuthu and A. Cuenat, *Colloids Surf. A*, 2011, **387**, 35–42.
- 16 M. Berka and J. A. Rice, *Langmuir*, 2005, **21**, 1223–1229.
- 17 A. A. Keller, H. Wang, D. Zhou, H. S. Lenihan, G. Cherr, B. J. Cardinale, R. Miller and Z. Ji, *Environ. Sci. Technol.*, 2010, **44**, 1962–1967.
- 18 L. Chekli, M. Roy, L. D. Tijning, E. Donner, E. Lombi and H. K. Shon, *J. Environ. Manage.*, 2015, **159**, 135–142.
- 19 E. Topuz, J. Traber, L. Sigg and I. Talinli, *Environ. Pollut.*, 2015, **204**, 313–323.
- 20 M. Luo, Y. Huang, M. Zhu, Y. Tang, T. Ren, J. Ren, H. Wang and F. Li, *J. Saudi Chem. Soc.*, 2016, 10.1016/j.jscs.2016.01.007.
- 21 F. Loosli, P. Le Coustumer and S. Stoll, *J. Nanoparticle Res.*, 2015, **17**, 44.
- 22 R. A. French, A. R. Jacobson, B. Kim, S. L. Isley, R. L. Penn and P. C. Baveye, *Environ. Sci. Technol.*, 2009, **43**, 1354–1359.
- 23 V. Adam, S. Loya-Lawniczak, J. Labille, C. Galindo, M. del Nero, S. Gangloff, T. Weber and G. Quaranta, *J. Nanoparticle Res.*, 2016, **18**, 13.
- 24 P. Vikesland, R. Rebodos, J.-Y. Bottero, J. Rose and A. Masion, *Environ. Sci. Nano*, 2016, **3**, 567–577.
- 25 H. Holthoff, S. U. Egelhaaf, M. Borkovec, P. Schurtenberger and H. Sticher, *Langmuir*, 1996, **12**, 5541–5549.
- 26 X. Liu, G. Chen and C. Su, *J. Colloid Interface Sci.*, 2011, **363**, 84–91.
- 27 W. Sutherland, *Philos. Mag. Ser. 6*, 1905, **9**, 781–785.
- 28 C. Nickel, J. Angelstorf, R. Bienert, C. Burkart, S. Gabsch, S. Giebner, A. Haase, B. Hellack, H. Hollert, K. Hund-Rinke, D. Jungmann, H. Kaminski, A. Luch, H. M. Maes, A. Nogowski, M. Oetken, A. Schaeffer, A. Schiwy, K. Schlich, M. Stintz, F. von der Kammer and T. A. J. Kuhlbusch, *J. Nanoparticle Res.*, 2014, **16**, 2260.
- 29 H. Moosmüller and W. P. Arnott, *J. Air Waste Manage. Assoc.*, 2009, **59**, 1028–1031.
- 30 A. Albanese and W. C. W. Chan, *ACS Nano*, 2011, **5**, 5478–5489.
- 31 N. Hondow, R. Brydson, P. Wang, M. D. Holton, M. R. Brown, P. Rees, H. D. Summers and A. Brown, *J. Nanoparticle Res.*, 2012, **14**, 977.
- 32 Z. Ji, X. Jin, S. George, T. Xia, H. Meng, X. Wang, E. Suarez, H. Zhang, E. M. V. Hoek, H. Godwin, A. E. Nel and J. I. Zink, *Environ. Sci. Technol.*, 2010, **44**, 7309–7314.
- 33 V. Filipe, A. Hawe and W. Jiskoot, *Pharm. Res.*, 2010, **27**, 796–810.
- 34 M. E. Mackay, A. Tuteja, P. M. Duxbury, C. J. Hawker, B. Van Horn, Z. Guan, G. Chen and R. S. Krishnan, *Science*, 2006, **311**, 1740–1743.
- 35 M. A. Kiser, P. Westerhoff, T. Benn, Y. Wang, J. Pérez-Rivera and K. Hristovski, *Environ. Sci. Technol.*, 2009, **43**, 6757–6763.
- 36 Y.-G. Zhou, N. V. Rees and R. G. Compton, *Angew. Chemie Int. Ed.*, 2011, **50**, 4219–4221.
- 37 N. V. Rees, *Electrochem. Commun.*, 2014, **43**, 83–86.
- 38 X. Xiao and A. J. Bard, *J. Am. Chem. Soc.*, 2007, **129**, 9610–9612.
- 39 W. Cheng and R. G. Compton, *Trends Anal. Chem.*, 2014, **58**, 79–89.
- 40 M. Pumera, *ACS Nano*, 2014, **8**, 7555–7558.
- 41 S. V. Sokolov, S. Eloul, E. Kätelhön, C. Batchelor-McAuley and R. G. Compton, *Phys. Chem. Chem. Phys.*, 2017, **58**, 79–89.
- 42 Y.-G. Zhou, N. V. Rees, J. Pillay, R. Tshikhudo, S. S. Vilakazi and R. G. Compton, *Chem. Commun.*, 2012, **48**, 224–226.
- 43 E. J. E. Stuart, N. V. Rees, J. T. Cullen and R. G. Compton, *Nanoscale*, 2013, **5**, 174–177.
- 44 W. Cheng, C. Batchelor-McAuley and R. G. Compton, *ChemElectroChem*, 2014, **1**, 714–717.
- 45 K. Shimizu, K. Tschulik and R. G. Compton, *Chem. Sci.*, 2016, **7**, 1408–1414.
- 46 J. C. Lees, J. Ellison, C. Batchelor-McAuley, K. Tschulik, C. Damm, D. Omanović and R. G. Compton, *ChemPhysChem*, 2013, **14**, 3895–3897.
- 47 C. Batchelor-McAuley, J. Ellison, K. Tschulik, P. L. Hurst, R. Boldt and R. G. Compton, *Analyst*, 2015, **140**, 5048–5054.
- 48 S. V. Sokolov, T. R. Bartlett, P. Fair, S. Fletcher and R. G. Compton, *Anal. Chem.*, 2016, **88**, 8908–8912.
- 49 H. S. Toh and R. G. Compton, *ChemistryOpen*, 2015, **4**, 261–263.
- 50 N. V. Rees, Y.-G. Zhou and R. G. Compton, *Chem. Phys. Lett.*, 2012, **525–526**, 69–71.
- 51 B. J. Plowman, N. P. Young, C. Batchelor-McAuley and R. G. Compton, *Angew. Chemie Int. Ed.*, 2016, **55**, 7002–7005.
- 52 Q. Lin and R. G. Compton, *J. Phys. Chem. C*, 2015, **119**, 23463–23469.
- 53 M. Thompson, G. G. Wildgoose and R. G. Compton, *ChemPhysChem*, 2006, **7**, 1328–1336.
- 54 T. R. Bartlett, S. V. Sokolov and R. G. Compton, *ChemistryOpen*, 2015, **4**, 600–605.
- 55 K. Tschulik and R. G. Compton, *Phys. Chem. Chem. Phys.*, 2014, **16**, 13909–13913.

- 56 K. Shimizu, S. V. Sokolov and R. G. Compton, *Colloid Interface Sci. Commun.*, 2016, **13**, 19–22.
- 57 J. Ellison, K. Tschulik, E. J. E. Stuart, K. Jurkschat, D. Omanovic, M. Uhlemann, A. Crossley and R. G. Compton, *ChemistryOpen*, 2013, **2**, 69–75.
- 58 N. V. Rees, Y.-G. Zhou and R. G. Compton, *ChemPhysChem*, 2011, **12**, 1645–1647.
- 59 Y.-G. Zhou, N. V. Rees and R. G. Compton, *Angew. Chemie Int. Ed.*, 2011, **50**, 4219–4221.
- 60 S. V. Sokolov, E. Kätelhön and R. G. Compton, *J. Phys. Chem. C*, 2015, **119**, 25093–25099.
- 61 Y. T. He, J. Wan and T. Tokunaga, *J. Nanoparticle Res.*, 2007, **10**, 321–332.
- 62 D. L. Sparks, *Elements*, 2007, **1**, 193–198.
- 63 R. Adams, *Focus Pigment.*, 2016, **2016**, 1–3.
- 64 G. Sørensen, C. H. Fischer, S. Bähring, K. P. Almqvist, K. Tønning, S. H. Mikkelsen and F. Christensen, *Occurrence and Effects of Nanosized Anatase Titanium Dioxide in Consumer Products*, Copenhagen, 2014.
- 65 B. O'Regan and M. Grätzel, *Nature*, 1991, **353**, 737–740.
- 66 K. Xu, A. Chatzidakis and T. Norby, *Photochem. Photobiol. Sci.*, 2016, 10.1039/C6PP00217J.
- 67 J. Meng, P. Zhang, F. Zhang, H. Liu, J. Fan, X. Liu, G. Yang, L. Jiang and S. Wang, *ACS Nano*, 2015, **9**, 9284–9291.
- 68 D. T. Sponza and R. Oztekin, *Environ. Technol.*, 2016, **37**, 865–879.
- 69 B. Liu, B. Chen, K. Lee, B. Zhang, Y. Ma and L. Jing, *Water Qual. Res. J. Canada*, 2016, **51**, 246–255.
- 70 B. D. Johnston, T. M. Scown, J. Moger, S. A. Cumberland, M. Baalousha, K. Linge, R. van Aerle, K. Jarvis, J. R. Lead and C. R. Tyler, *Environ. Sci. Technol.*, 2010, **44**, 1144–1151.
- 71 Q. Fang, X. Shi, L. Zhang, Q. Wang, X. Wang, Y. Guo and B. Zhou, *J. Hazard. Mater.*, 2015, **283**, 897–904.
- 72 W.-S. Cho, B.-C. Kang, J. K. Lee, J. Jeong, J.-H. Che and S. H. Seok, *Part. Fibre Toxicol.*, 2013, **10**, 9.
- 73 R. Anton, S. Barlow, D. Boskou, L. Castle, R. Crebelli, W. Dekant, K.-H. Engel, S. Forsythe, W. Grunow, M. Heinonen, J. C. Larsen, C. Leclercq, W. Mennes, M.-R. Milana, I. Pratt, I. Rietjens, K. Svensson, P. Tobback and F. Toldrá, *EFSA J.*, 2005, **163**, 1–12.
- 74 D. L. Jacob, J. D. Borchardt, L. Navaratnam, M. L. Otte and A. N. Bezbaruah, *Int. J. Phytoremediation*, 2013, **15**, 142–153.
- 75 M. A. Maurer-Jones, I. L. Gunsolus, C. J. Murphy and C. L. Haynes, *Anal. Chem.*, 2013, **85**, 3036–3049.
- 76 K. Hirakawa, M. Mori, M. Yoshida, S. Oikawa and S. Kawanishi, *Free Radic. Res.*, 2004, **38**, 439–447.
- 77 H. Goto, Y. Hanada, T. Ohno and M. Matsumura, *J. Catal.*, 2004, **225**, 223–229.
- 78 A. Turcanu and T. Bechtold, *Dye. Pigment.*, 2011, **91**, 324–331.
- 79 H.-P. Dai and K.-K. Shiu, *Electrochim. Acta*, 1998, **43**, 2709–2715.
- 80 I. A. Mudunkotuwa and V. H. Grassian, *J. Am. Chem. Soc.*, 2010, **132**, 14986–14994.
- 81 P. T. Hang and G. W. Brindley, *Clays Clay Miner.*, 1970, **18**, 203–212.
- 82 G. Kahr and F. T. Madsen, *Appl. Clay Sci.*, 1995, **9**, 327–336.
- 83 L. Pauling, *The Nature of the Chemical Bond and the Structure of Molecules and Crystals: an Introduction to Modern Structural Chemistry*, Cornell University Press, New York, 3rd Ed., 1960.
- 84 E. Kätelhön, E. E. L. Tanner, C. Batchelor-McAuley and R. G. Compton, *Electrochim. Acta*, 2016, **199**, 297–304.
- 85 K. Tschulik, B. Haddou, D. Omanović, N. V. Rees and R. G. Compton, *Nano Res.*, 2013, **6**, 836–841.
- 86 G. H. Brimhall and W. E. Dietrich, *Geochim. Cosmochim. Acta*, 1987, **51**, 567–587.
- 87 E. Limpert, W. A. Stahel and M. Abbt, *Bioscience*, 2001, **51**, 341–352.
- 88 R. G. Compton and C. E. Banks, *Understanding Voltammetry*, London, 2nd Ed., 2011.
- 89 A. J. Bard and L. R. Faulkner, *Electrochemical Methods: Fundamentals and Applications*, John Wiley & Sons, New York, 2nd Ed., 2001.
- 90 N. Tanjila, A. Rayhan, M. S. Alam, I. A. Siddiquey and M. A. Hasnat, *RSC Adv.*, 2016, **6**, 93162–93168.
- 91 E. Laviron, *J. Electroanal. Chem.*, 1974, **52**, 355–393.
- 92 E. A. Dada and L. A. Wenzel, *Ind. Eng. Chem. Res.*, 1991, **30**, 396–402.
- 93 B. Haddou, N. V. Rees and R. G. Compton, *Phys. Chem. Chem. Phys.*, 2012, **14**, 13612–13617.